Applications in Energy and Combustion Science 26 (2026) 100482

Contents lists available at ScienceDirect

Applications in Energy and Combustion Science

journal homepage: www.elsevier.com/locate/jaecs

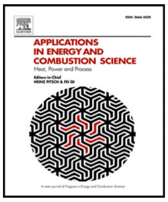

Flashback prevention in a hydrogen-fueled original micro Gas Turbine without any combustor redesign: Large-Eddy Simulation verification of a strategy based on 0D/1D predictions

Alessio Pappa [a,b,*], Laurent Bricteux [a], Ward De Paepe [a,b,c]

[a] University of Mons (UMONS), Faculty of Engineering, Mechanical Department, Mons, 7000, Belgium
[b] UMARC - UMONS Micro gAs turbine Research Center, Mons, 7000, Belgium
[c] WEL Research Institute, avenue Pasteur 6, Wavre, 1300, Belgium

ARTICLE INFO

Keywords:
Large-Eddy Simulation (LES)
Turbulent combustion
micro Gas Turbine (mGT)
Hydrogen
Flashback
Humidification
Exhaust Gas Recirculation (EGR)

ABSTRACT

Premixed burners, commonly used in micro Gas Turbines (mGT), are prone to flame instabilities when fueled with hydrogen or hydrogen blends. Humidification and Exhaust Gas Recirculation (EGR) provide solutions to prevent flashback in an mGT burner without requiring any combustor redesign. Currently, these solutions are rarely considered, and no prediction methodology exists. Therefore, a low-complexity method using a hybrid 0D/1D model was proposed in previous work to predict the dilution levels necessary to prevent flashback, based on an easily accessible parameter, the laminar flame speed. This work aims to verify the potential of humidification and EGR, as well as the predicted dilution levels generated by the 0D/1D model, through high-fidelity simulations.

To achieve this, Large-Eddy Simulations (LES) of an original mGT combustor layout are performed using a complex chemistry approach with an Adaptive Mesh Refinement methodology. These simulations compare pure methane combustion, considered as a reference case, to a case with a CH_4/H_2 blend of 50/50%$_{vol}$, highlighting flashback, and to cases that implement solutions to limit this flashback — such as humidification and EGR — for different hydrogen fractions, 50% and 100%. The numerical results show that flashback is prevented in all solution cases. The 50% H_2 case with humidification exhibits behavior most similar to the reference case. Whereas the EGR case results in a longer and colder flame, the case with 100 %H_2 plus water shows a shorter, more reactive flame with a high turbulent flame speed near the flame foot, indicating conditions near the limit of flashback disruption.

1. Introduction

Given the non-dispatchable and intermittent nature of renewable energy sources, hydrogen as a clean energy carrier can provide a suitable solution to store the excess of electricity coming from renewable energies, i.e. using Power-to-Gas to convert by electrolysis this excess renewable electricity into the so-called “Green hydrogen” [1]. For the reconversion of this green H_2 into electricity, combustion-based technologies, such as Gas turbines (GTs) and micro Gas Turbines (mGTs), remain efficient and reliable technologies [2]. Especially in a decentralized production with cogeneration, mGT technologies offer great advantages related to their high adaptability and flexibility, in terms of operation and fuel [3]. Nevertheless, lean premixed (typical configuration in GTs or mGTs) hydrogen/air flames feature well-known flame instabilities, such as intrinsic instabilities at a smaller scale, and flashback at a larger scale. The high temperatures and reaction rates reached in the combustor can potentially lead to a fast upstream traveling of the flame front due to a flame speed larger than the bulk speed, potentially causing major and irreversible damage to the facility.

To achieve a stable and controlled hydrogen-firing combustion, especially with 100 % H_2 fueling as a target, three main strategies stand out in literature: many small rich diffusion flames (bundle-burners, multi-cluster, or micromix) [4,5], co-axial staging (stabilized propagation using advanced aerodynamics) [6], and longitudinal or axial staging for sequential combustion (controlling the ignition time and firing temperature in the first stage, and stabilizing the flame in the second stage) [7]. The main conclusion from the literature is that hydrogen combustion, especially pure hydrogen combustion, typically requires a combustor redesign. This combustor redesign consists of modifying

---

[*] Correspondence to: Rue de l’Epargne 56, 7000 Mons, Belgium.
E-mail address: alessio.pappa@umons.ac.be (A. Pappa).

https://doi.org/10.1016/j.jaecs.2026.100482
Received 12 December 2025; Received in revised form 27 February 2026; Accepted 27 February 2026

the injector configuration or layout. Thus, the final combustors are or might be no longer suitable for other fuels, such as H_2 blends, natural gas, or biogas, limiting the fuel and operational flexibility of the gas turbine. Although a complete and stable combustion at $100\,\%$ H_2 firing is possible, as shown in the literature by these few examples of existing solutions involving a redesign, the maximal hydrogen fraction experimentally tested in a mGT without any redesign of its combustor is around $20\,\%$ in a $3\,kW_e$ mGT [8]. To reach $100\,\%$ H_2 in a $100\,kW_e$ mGT, Banihabib et al. [9] had to propose a complete redesign of the mGT combustor, integrating FLOX® (flameless oxidation) nozzles [10,11] to the original combustor design. This combustor design enabled this $100\,kW_e$ mGT to be the first successful mGT tested running on 100% hydrogen with NO_x emissions below the standard limits, still offering fuel flexibility.

In a context of increasing fuel flexibility with small-scale cogeneration units, development must focus on one specific chamber, designed and adapted for various fuels and operating conditions. So far, an alternative solution to avoid any redesign of the combustor stands in using diluted combustion air to slow down the reaction. Hence, this work aims at stabilizing hydrogen combustion in mGTs without any combustor redesign. The ambition is thus to demonstrate the viability of flame stabilization methods under diluted conditions, stemming from modifications to the mGT advanced cycle, such as humidification and Exhaust Gas Recirculation (EGR). Usually considered as a negative effect, performing air humidification or EGR alters the combustor inlet conditions, slowing down the flame speed and reducing the reaction rate and temperature, as shown several times in the literature [12–17]. The work of Stathopoulos et al. [18] can be highlighted for the experimental demonstration of steam injection for increased flashback safety in a swirl-stabilized high-pressure combustor. However, using EGR for the dilution effect of CO_2 and N_2 for flashback limitation has not yet been tested numerically or experimentally. Nevertheless, despite the real difficulty to emulate a large recirculation of exhaust gases (still too barely developed on a real mGT), we can highlight some works which are assessing the CO_2 dilution effect on CH_4/H_2 blends. The experimental work of du Toit et al. [16] has shown a NO_x emission reduction, while Hasti et al. [17] have numerically observed, using Large-Eddy Simulations (LES), the effect of CO_2 dilution on the flame shape, showing longer but less wrinkled flames.

Besides this potential in reducing the chance of flashback apparition, humidification enables increasing the mGT electric efficiency by increasing the specific heat capacity [19], and EGR enables reducing the penalty cost when performing carbon capture by increasing the CO_2 content in the exhaust gases [20]. Nevertheless, these dilution solutions, with both advantages — the positive impact on the mGT cycle and potential flashback limitation — are currently little considered, and no prediction methodology for the dilution levels of humidification or EGR aiming at limiting flashback exists. Up to now, we can only highlight the work of Pousada et al. [21] which recently presented a model based on LES with a thickened flame model for flashback limitation using water injection in a high pressure GT, using optimization of the operating conditions based on Global Sensitivity Analysis (GSA) with a surrogate model.

To fill this research gap, and in the continuity of a previous paper [22], our work aims at stabilizing hydrogen combustion in mGTs without any combustor redesign, using humidification and EGR to prevent flashback. As there was no prior indication on which dilution levels to be used to prevent flashback, and we aimed to avoid using significant amount of numerical resources to perform CFD at random operating conditions, a first paper [22], being the first part of our work, focused on a methodology for fast and low-complexity predictions of the dilution level to prevent flashback based on an easy-to-get parameter, the laminar flame speed. To do so, a parametric study over a specific range of operating conditions of the Turbec T100 mGT [23] combustor was presented. Using a hybrid combustor model (low complexity and computationally fast model), combining a 0D Chemical Reactor Network (CRN) with 1D laminar flame calculations, the necessary minimal water amount or EGR ratio is assessed and optimized to reach the same level of laminar flame speed as reached in classical pure methane combustion. This methodology also allows for predicting the combustion temperature and emissions at a reduced cost. The 0D/1D analysis shows that a CH_4/H_2 blend of $50/50\%_{vol}$ requires either a water-to-air ratio of $\Omega = 3.4\,\%$, or an EGR ratio of $77\,\%$ for flame stabilization. Burning up to $100\,\%$ H_2 involves $\Omega = 10.25\,\%$, while no solution exists when performing EGR.

This proposed low computational cost model aims at offering a calculated estimation of the condition to avoid flashback involving a fast and low-complexity tool for any mGT operator, based on an easy-to-get criterion, the laminar flame speed. In this previous paper [22], we discussed the choice and pointed out the limitations of this simplified criterion. Based on the literature, there could indeed be more refined parameters, including turbulence and flame dynamics. Hence, as a second step of our work, this paper focuses on the verification with high-fidelity simulations, using LES with complex chemistry of the actual combustor geometry of the T100 mGT to verify whether the previous 0D/1D predictions lead to flashback limitation.

In this paper, the combustor layout and operating conditions are first described, followed by a detailed description of the numerical setup. Then, the results section features a verification of the numerical results with available data, a qualitative analysis of the combustion performances, a stability analysis of the different combustion regimes, and finally, a discussion about the effect of turbulence on the flame front to confront laminar and turbulent flame speeds, and verify the statement of the proposed strategy oriented to the laminar flame speed.

2. Combustor layout & operating conditions

The combustion chamber considered for the simulations is the one of the Turbec T100 mGT [23]. At nominal operating conditions, this mGT produces a net electrical power output of $100\,kW_e$. The Turbec T100 mGT operates using the recuperated Brayton cycle, meaning that the dry air is first compressed by the variable speed compressor. Then the compressed air is preheated up to $865\,K$ in the recuperator using the heat from the exhaust gases before entering the combustion chamber to be heated further till $1225\,K$ by burning natural gas. The T100 combustor itself features a can swirl burner (or counter-current flow, see Fig. 1) where the combustion air is entering between the outer casing and the inner walls of the combustor. The air reaches then the dilution holes, the pilot and main injectors by passing on the external surface of the inner walls.

The layout characteristics of this combustor are (Fig. 1): a pilot flame exploiting a diffusion flame, fed by 12 air injectors and 6 fuel injectors; a premixed combustion as main flame using two rows of swirler (a first one to premix fuel and air, and a second one to enhance the flow momentum ending with 30 swirled injectors); and 9 dilution holes to cool down the exhaust gases to avoid any damages at the turbine inlet.

The operating conditions of the Turbec T100 mGT at the nominal point for classical pure methane combustion, considered as reference case (Ref case), are presented in Table 1. The thermal power remains constant for all simulated cases. When the mGT operates with hydrogen-firing, flashback is most likely to appear in the premixing zone of the main injectors from $20–25\%_{vol}$ H_2 as observed experimentally by Tuncer et al. [24].

The operating conditions of the cases that will be simulated in this paper are selected based on the results provided by the hybrid 0D/1D analysis presented in [22]. Pure methane combustion, considered as the reference case, will be compared to a case for which the operating conditions lead to flashback (FB case) involving a CH_4/H_2 blend of $50/50\%_{vol}$, and to cases with a solution to limit flashback for different hydrogen fractions, 50% and 100%. Among the considered solution cases, for a CH_4/H_2 blend of $50/50\%_{vol}$, we are comparing

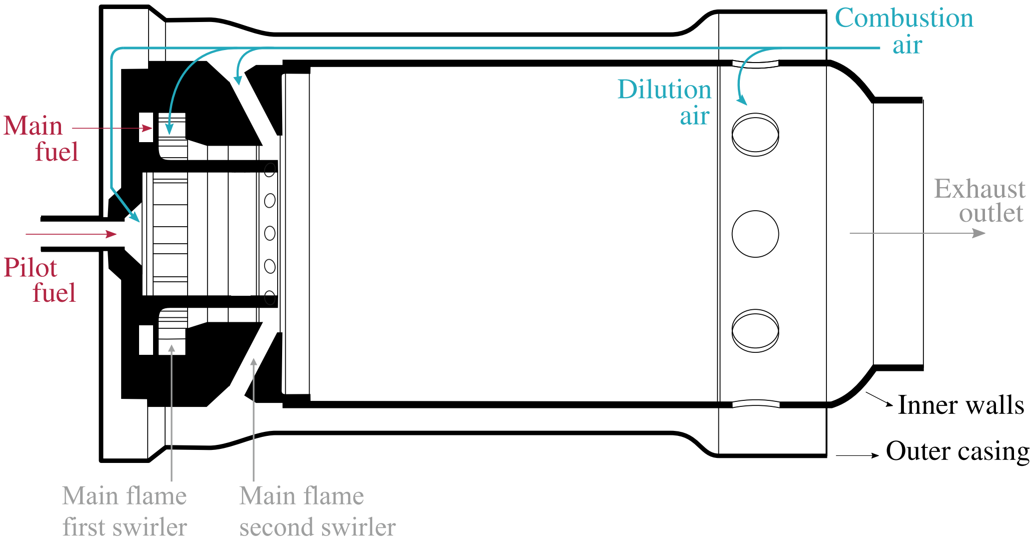

Fig. 1. The Turbec T100 combustion chamber is a reverse (or counter-current) flow can burner.

Table 1
Operating conditions of the Turbec T100 mGT at nominal operating point for a classical pure methane combustion, considered as reference case (Ref case).

Net electrical power output, P_e	100 kW$_e$
Fuel consumption, P_{th}	333 kW$_{th}$
Air mass flow rate, $\dot{m}_{air}$	800 g s^{-1}
Pressure in the combustor, p	4 bar
Inlet air temperature, T_{in}	865 K
Inlet fuel temperature, T_{in}	300 K
Global equivalence ratio, ϕ_{global}	0.14
Local main flame equivalence ratio, ϕ_{main}	0.41

3 different solutions: an oxidizer temperature decrease (50H_2LT case), a humidified case (50$H_2\Omega$), and an EGR case (50H_2EGR case). Finally, a 100% H_2 case is also simulated under humidified conditions (100$H_2\Omega$). The hybrid 0D/1D analysis presented in [22] shows that a CH_4/H_2 blend of 50/50%$_{vol}$ requires a water-to-air ratio of 3.4 %, or at least an oxidizer temperature decrease of 60 °C, to ensure stable combustion. When performing EGR, a ratio of 77 % is needed for this fuel mixture, while no solution exists for 100 % H_2. This limit within the hydrogen fraction to around 55 % when performing EGR is related to the EGR cycle itself. As detailed in [22], the model for the EGR case is constructed such that the exhaust gases are recirculated, cooled, and dried (i.e., water is removed). Consequently, the main species contributing to combustion dilution is N_2 together with a fixed and limited amount of residual water and CO_2, whose concentration rapidly decreases as the hydrogen fraction increases. This leads to an already high EGR ratio of 77% at 55% H_2, which is close to the technical limits on achievable EGR levels. Combustion air humidification shows a major advantage by allowing it to burn up to 100 % of H_2, requiring a water-to-air ratio of 10.25 %. The defined simulated cases are summarized in Table 2. The details on composition and comparison between different processes to perform humidification and EGR are presented in [22]. In the previous study [22], the comparisons and conclusions have led to consider dry cooled EGR (exhaust gases cooled down to 30 °C and water condensed and removed), and to inject water at 450 K using a saturation tower.

3. Numerical set-up

The LES, presented in this paper, are performed using the massively parallel flow solver YALES2 [25]. This finite-volume code solves the low-Mach number Navier–Stokes equations using a projection method [26] for variable density flows [27]. Equations are solved using a 4 th order centered scheme in space and a 4 th order TFV4 A scheme in time [28] (low-storage RK4 blended with Lax Wendroff-type scheme) for high precision. The numerical code has been validated several times for different configurations [29,30]. Especially, the validated LES of the lean-premixed Preccinsta burner with wall heat loss is comparable to the cases presented in this paper [31]. The turbulent sub-grid scale stresses are modeled with the local dynamic Smagorinsky model [32]. The stability of the time integration is ensured with an adaptive time step that keeps the CFL number under 0.4. The species diffusion velocity is modeled with the Hirschfelder and Curtiss approximation [33]. Moreover, the chosen operating conditions lead to a Reynolds Number $Re = 37500$ and a dimensionless wall distance $y^+ = 40$ in the main swirler. Therefore, we use a classical log-law profile as wall model [34] in our simulations. Adiabatic walls are considered (no heat losses).

The combustion is simulated by coupling finite-rate chemistry to a detailed chemical mechanism. The conservation equations for reacting flows (mass, species, momentum and energy) are solved by transporting all species and evaluating the source terms from the considered kinetic mechanism for our LES, the DRM19 [35] (21 species and 84 reactions). This reduced kinetic scheme has been chosen for its versatility to deal with the different operating conditions and fuel blends at a reduced computational cost. It has been compared to several kinetic schemes (from more complete to other reduced kinetic schemes) at the T100 mGT operating conditions in [14,22] using 0D/1D calculations on temperature, species, and ignition delays evolutions. In addition, to avoid constraints imposed by the limited chemical time step an operator splitting method [36] is used relying on stiff integration of ordinary differential equations solver CVODE [37].

A combustion model of artificially thickened flame is used to correctly predict the combustion and to model the sub-grid scale turbulence/chemistry interaction on the LES grid. In our LES, the dynamic Thickened Flames model (TFLES) [38] is implemented by modifying the conservation equations with a thickening factor F and the efficiency function E of Charlette et al. [39] (considering a static formulation with $\beta = 0.5$), to have the thermal flame thickness $\delta_T = F \cdot \delta_L^0$ and flame speed $S_T^0 = E \cdot S_L^0$ where S_T^0 is the sub-grid scale turbulent flame speed [40]. A flame sensor is employed to activate locally and dynamically the flame thickening to obtain 5 points mesh resolution in the flame front. This flame sensor is based on the source term of a virtual progress variable c, and excluding heat release points with a value under 10 % of the maximum HRR $\dot{\omega}_{c,max}$. This progress variable is computed as $c = Y_c / Y_{c,eq}$, where $Y_c = Y_{CO_2} + Y_{CO} + Y_{H_2O}$ and $Y_{c,eq}$ is Y_c at chemical equilibrium.

Table 2
Cases considered for the LES simulations with the description of their operating conditions.

Case name	Fuel	Dilution	Operating conditions
Ref	100$\%_{vol}$ CH_4	–	Nominal conditions of the Turbec T100
FB	50$\%_{vol}$ CH_4/50$\%_{vol}$ H_2	–	Nominal conditions of the Turbec T100
50H_2LT	50$\%_{vol}$ CH_4/50$\%_{vol}$ H_2	–	Premixed flow temp. = 760 K (instead of 830 K)
50$H_2\Omega$	50$\%_{vol}$ CH_4/50$\%_{vol}$ H_2	$\Omega = 3.4\%$	Nominal conditions of the Turbec T100
50H_2EGR	50$\%_{vol}$ CH_4/50$\%_{vol}$ H_2	$EGR = 77\%$	Nominal conditions of the Turbec T100
100$H_2\Omega$	100$\%_{vol}$ H_2	$\Omega = 10.25\%$	Nominal conditions of the Turbec T100

In addition, an Adaptive Mesh Refinement (AMR) algorithm is used for the LES simulations [41]. By dynamically refining the mesh in the flame region, based on a combustion criterion using the flame sensor of the TFLES model, the mesh is optimized in terms of cell quantity and distribution. The AMR algorithm dynamically refines the mesh all along the flow simulation to lead to the LES mesh. The flame sensor detects the region of the domain where the heat release value is higher than a reference value (defining where the combustion occurs). Then, a triggering adaptation strategy, based on an error metric-based strategy (triggered at each $\epsilon > \epsilon_{max}$), allows refining the region where fluctuations are observed according to the defined target metrics. In addition, a security margin is used by the algorithm in terms of cell number surrounding the flame. The number of propagating cells around the flame is set for two reasons. First, it ensures that any unexpected flame fluctuation is always captured by the refined mesh area. Then, it avoids unnecessary refinement during the resolutions. Indeed, by surrounding the potential flame fluctuations, it avoids refining too often, limiting thus the CPU cost contribution of the AMR. For the validation and the full details of the AMR methodology, the reader is invited to read [41–44]. This method enables the mesh to be refined only in areas where finer cells are needed to capture important phenomena, such as the flame front, automatically resulting in an optimized mesh and reducing manual meshing effort.

The automatically refined mesh obtained for the LES simulations includes a ranging number of cells from 60 to 80 million tetrahedral cells (depending on the case), where the size of the cells ranges from $\Delta = 700\,\mu\text{m}$ ($\Delta/D = 5.26 * 10^{-3}$, with D the diameter of the combustor, and $\Delta/\delta_L^0 = 2.6$) in the flame front region to $\Delta = 3\,\text{mm}$ ($\Delta/D = 22.6 * 10^{-3}$, and $\Delta/l_t = 0.36$) in the domain. The cell size in the flame front is set to limit the thickening factor to a maximum of 12. It is globally set at the lowest possible values to maintain a good balance between accuracy and computational cost for the six considered cases. The AMR has an impact on the total CPU cost. It represents 1 to 3% of the total CPU load.

For all cases, the simulation ran over 2 through flow times τ_{tf} (time needed for the flow to cross the combustion chamber divided by the residence time) to ensure that the flow is well established. An additional 3 τ_{tf} were used to obtain the statistics presented in this paper. The total of 5 τ_{tf} required 576 kCPUh.

4. Results and discussions

This section presents the obtained LES results, where the six considered cases are compared to verify whether the predetermined operating conditions of the solution cases lead to a stable and safe combustion.

4.1. Model verification

A proper validation would require flow field measurements of the flame region to fully validate the LES results. However, this is unfortunately technically impossible and has never been achieved in a real facility with a complete running mGT, since there is no option for optical access, nor for detailed measurement of temperature, species, or velocity. Nevertheless, there is still the option to validate the outlet conditions of the Ref case at nominal conditions. The LES results are thus compared with data available from the datasheet of the Turbec T100 [23], experimental measurements of the outlet flow conditions for the Ref case [45], and the results provided by our 0D/1D model [22]. The LES results presented in Table 3 are the time- and space-averaged values at the combustor outlet. The comparison shows that the Turbine Inlet Temperature and the O_2, CO_2 and CO emissions predicted by both the 0D/1D model and the LES differ from the experimental data by less than 1%. This agreement indicates that the global thermochemical balance at the combustor exit is reasonably captured by the numerical model, even though this level of validation does not guarantee the accuracy of the predicted local flame structure, turbulence–chemistry interaction, or detailed flow features inside the combustor.

Table 3
Comparison of the 0D/1D and LES results for the combustor outlet conditions with experimental data for the Ref case, showing similar outcomes for the TIT, and molar fractions of the O_2, CO_2 and CO emissions.

	Datasheet [23]	Experimental [45]	0D/1D [22]	LES
T [K]	1220	1207.4 ± 12	1201	1205.7
X_{O_2} [$\%_{vol}$]	–	17.53 ± 0.2	17.67	17.55
X_{CO_2} [$\%_{vol}$]	–	1.46 ± 0.04	1.47	1.5
X_{CO} [ppmv]	<15	3 ± 5	0	4

Only the outlet conditions of the Ref case can be validated with experimental data, since the other presented cases have never been attempted on the actual Turbec T100 mGT facility, or any other facility of its kind. Hence, the LES results are compared to the results from our 0D/1D model for a cross-validation in Table 4 by calculating the relative discrepancy ϵ for the TIT, and molar fractions of O_2, H_2O and CO_2. This relative discrepancy does not exceed 1.5% for the TIT, and 4% for the O_2 molar fraction, while the highest relative discrepancies are reached by the H_2O and CO_2 molar fractions. Considering the technical limitations to obtain detailed experimental data for all the studied cases, it can be acknowledged that the LES results are within a fairly realistic range, and the present assessment should therefore be regarded as a partial validation. This assessment against available data brings some confidence in analyzing the results for this first essential step in fueling an actual mGT burner with hydrogen.

4.2. Flashback phenomenology

The fast upstream traveling of the flame front across the injector occurring during flashback follows one of these three distinctive mechanisms [46,47]: the thermo-acoustic flashback, the boundary layer flashback, or the core flow flashback. The thermo-acoustic flashback is caused by pulsating pressure oscillation due to thermo-acoustic instabilities, which leads to pulling the flame back into the injector. The boundary layer flashback is due to a velocity deficit of the bulk flow at the injector wall. Finally, the core flow flashback is created by an expected or unexpected swirled flow inside a channel-shaped injector, creating a vortex that stretches the flow centerline to the upstream.

As shown in Fig. 2, which compares the passive scalar Z of the oxidizer/fuel mixture fraction between the Ref and the FB cases, boundary layer flashback is the dominant mechanism in the Turbec T100 combustor. This passive scalar is a mixture fraction based on atomic conservation transported on the Eulerian grid. This mixture fraction is calculated on the Bilger definition from the provided initial fuel and

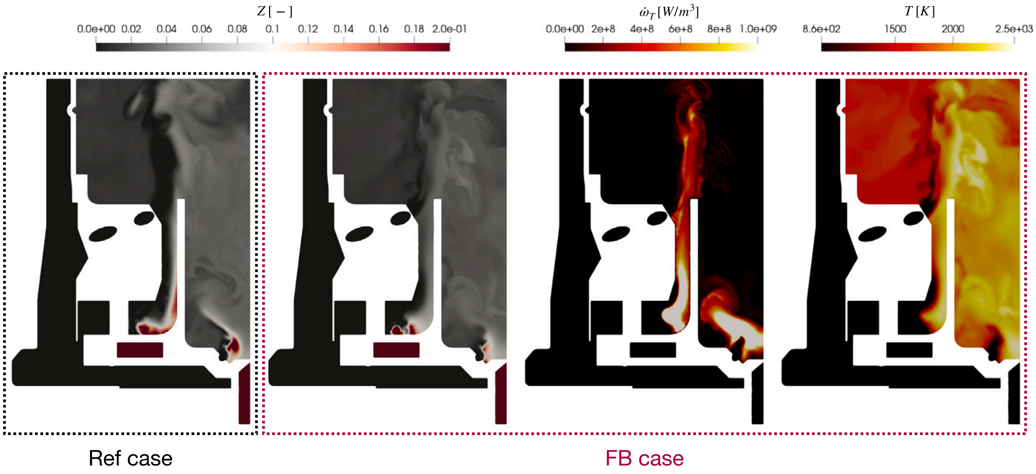

Fig. 2. LES results for the Ref case of the passive scalar of the mixture fraction Z compared to the Z field of the FB case, the instantaneous reaction rate $\dot{\omega}_T$ and the temperature color fields showing the boundary layer flashback apparition near the main flame swirler.

Table 4
Comparison for cross-validation between the reduced-order 0D/1D model and the LES results for the combustor outlet conditions for the FB, $50H_2LT$, $50H_2\Omega$, $50H_2EGR$, and $100H_2\Omega$ cases, showing the relative discrepancy for the TIT, and molar fractions of the O_2, H_2O, and CO_2.

		T[K]	X_{O_2} [$\%_{vol}$]	X_{H_2O} [$\%_{vol}$]	X_{CO_2} [$\%_{vol}$]
FB	0D/1D	1193.4	17.8	3.4	1.1
	LES	1199.8	17.2	4.1	1.4
	ϵ	0.5%	3.6%	16.3%	19.4%
$50H_2LT$	0D/1D	1151.8	17.8	3.4	1.1
	LES	1157.7	17.2	4	1.3
	ϵ	0.5%	3%	15.4%	16.3%
$50H_2\Omega$	0D/1D	1166.5	16.8	8.6	1.1
	LES	1167.3	16.5	8.6	1.3
	ϵ	0.1%	2.1%	0.4%	14.3%
$50H_2EGR$	0D/1D	1187.6	8.9	4.2	5.1
	LES	1170.2	8.7	4.6	4.8
	ϵ	1.5%	1.9%	9.1%	6.5%
$100H_2\Omega$	0D/1D	1119.7	15.1	19.7	0
	LES	1114.4	15.6	18	0
	ϵ	0.5%	3.4%	9.7%	0%

oxidizer composition. Indeed, the passive scalar Z fields clearly indicate a higher concentration of the fuel/oxidizer mixture near the inner wall. The Turbec T100 relies on two swirlers to support the main flame: the first premixes the fuel with the oxidizer, while the second enhances the momentum. The rapid expansion of the swirled air ensures effective mixing through the shear layer in the initial part of the injector and helps maintain the mixture along the inner walls. This process is further amplified by the second swirler, which helps create the flame front in the shear layer between the main and pilot flows. Ultimately, the instantaneous reaction rate $\dot{\omega}_T$ and the temperature color fields in the FB case reveal that the flame recedes from the upper flame front through the main injectors. The results indicate that flashback is not caused by auto-ignition in the premix chamber but by boundary layer flashback within the channel leading to the second swirler of the main flame.

While this conclusion remains valid, several aspects deserve further discussion. In the present simulations, the grid resolution ($y^+ = 40$) in the near-wall region is such that both the wall shear stress and the velocity profiles are modeled rather than resolved. One may thus question whether the identified flashback mechanism could differ from that occurring in the actual configuration. Nevertheless, when comparing our results with the three flashback mechanisms commonly reported in the literature, and considering the wall-modeled LES results that reveal a clear velocity deficit along the injector walls, the only mechanism consistent with our simulations is boundary-layer flashback, even though the boundary layers inside the injectors are modeled rather than fully resolved. Thermo-acoustic flashback cannot be captured in the present framework, since a variable-density solver is used. In addition, the injector geometry prevents the occurrence of core-flow flashback. From a numerical standpoint, the conclusion is therefore self-consistent within the assumptions and limitations of the model, although it may not fully reflect the behavior of the actual burner. In the real burner, a coupled mechanism involving both boundary-layer flashback and thermo-acoustic effects cannot be excluded, as pressure fluctuations during operation may promote flashback events. Assessing such combined mechanisms would require the use of a compressible flow solver.

In case of boundary layer flashback, as suggested in literature [48, 49], the upstream flame propagation occurs when the flow velocity gradient at the wall equals the ratio between the laminar flame speed and the flame thickness:

$$\frac{U}{d} \leq \frac{S_l^0}{\delta_l^0}, \tag{1}$$

where U is the bulk velocity and d is the space between the walls in the injector, while δ_l^0 and S_l^0 are respectively the laminar flame thickness and the laminar flame speed. This approach has been adapted in this paper by switching the laminar flame thickness δ_l^0 by the diffusive thickness δ, defined as:

$$\delta = \frac{D_{th}}{S_l^0}, \tag{2}$$

with D_{th} the thermal diffusivity in fresh gases. This leads to a flame *Propagation allowance* number (Pa), defined as:

$$Pa = \frac{U}{d} \cdot \frac{\delta}{S_l^0}, \tag{3}$$

with U representing the time-averaged velocity flow field in the swirler channel of the main flame, and d the spacing in the swirler channel where flashback is about to occur for $Pa < 1$. Fig. 3 shows the probability density of the Pa number calculated from the LES results for the FB case of points located in the premixing swirler of the main flame. The distribution of the Pa number indicates that most points are below the defined flashback threshold, with an average value of 0.73. However, all hydrogen combustion simulations in mGT combustors conducted by the author suggest that operating conditions can potentially lead to flashback events even when $1 < Pa < 2$. Finally, the calculated mean values of Pa in the main swirler for all cases are compared in Table 5, showing that all solution cases involve $Pa > 2$.

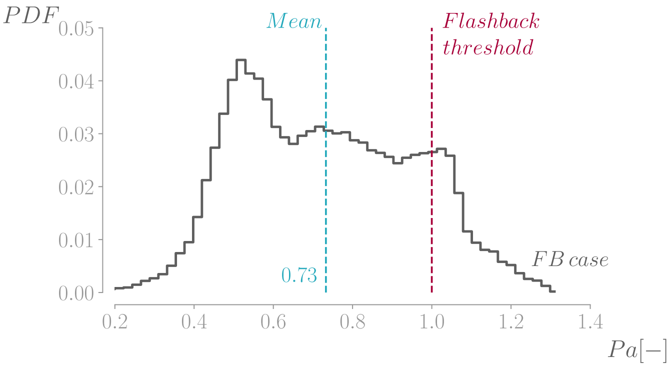

Fig. 3. Probability Density Function (PDF) of the Pa number for the flashback case (FB case), showing that most of the point in the main flame swirler are $Pa < 1$ with an average at $Pa = 0.73$.

Table 5
Mean values of Pa number for all simulated cases, showing that tha solution cases have values higher than the defined flashback threshold $Pa = 2$.

Cases	Pa [–]
Ref	4.96
FB	0.73
$50H_2LT$	4.98
$50H_2\Omega$	4.9
$50H_2EGR$	8.84
$100H_2\Omega$	4.8

4.3. Performance comparison

In this section, a qualitative analysis of the flame behavior is presented to determine whether flashback is truly avoided in cases where a dilution solution or temperature reduction is employed.

Consumption and heat release rates

The instantaneous H_2 source term $\dot{\omega}_{H_2}$ flow field distributions (Fig. 4(a)) and the time-averaged and fluctuating values of the HRR $\dot{\omega}_T$ flow fields (Fig. 4(b) and (c)), all made dimensionless by dividing it through the maximal time-averaged HRR of the Ref case, are used for a qualitative analysis. The H_2 source term fields (Fig. 4(a)) show where H_2 is produced (positive values in red) and consumed (negative values in blue). The negative values of the H_2 source term $\dot{\omega}_{H_2}$ consumption area provide thus an indication on the H_2 consumption rate of the different considered cases. The joint analysis of these quantities allows highlighting the main differences in the combustion process of the solution cases compared to the Ref and FB cases.

First, the flashback for the FB case is clearly confirmed by the H_2 consumption and peak of HRR in the main swirler, unlike in the solution cases. Then, these solution cases present a different behavior between themselves in the way of consuming the H_2. The H_2 source term flow field distributions of the $50H_2\Omega$ and $100H_2\Omega$ cases show a slightly larger region of H_2 consumption than the $50H_2LT$ and $50H_2EGR$ cases. However, these larger regions are not necessarily correlated with larger regions of high mean HRR, as for the $50H_2\Omega$ case. The time-averaged HRR distribution of the $50H_2\Omega$ case is actually similar to the one of the Ref case, with the same level of HRR fluctuations. Nevertheless, for the $100H_2\Omega$ case, the consumption zone of H_2 extends even further downstream compared to the location of the observed peak of mean and fluctuating HRR (in Fig. 4(b) and (c)), showing a thicker consumption area than the $50H_2\Omega$ case. Compared to the Ref case, both $50H_2LT$ and $50H_2\Omega$ cases show very similar time-averaged and fluctuating HRR flow fields, while both $50H_2EGR$ and $100H_2\Omega$ cases present the most different distribution. However, higher values of HRR fluctuation are generated by the $50H_2LT$ case, compared to the Ref and the solution cases fueled by $50\%_{vol}$ H_2, near the main injectors, potentially reducing the flame stability, while the dilution effect of water of the $50H_2\Omega$ smooths the fluctuations of HRR tending to the same distribution as for the Ref case. The EGR case presents the lowest values of consumption rate, and mean and fluctuating HRR in the flame region due to the high dilution level, facing a spatial delay in the oxidation of the reactants, and a lower reactivity. In opposition, the moderate level of dilution of the $100H_2\Omega$ case does not reach to shift the reaction point more downstream of the injectors. This narrow distribution near the injectors with higher peaks of time-averaged and fluctuations of the $100H_2\Omega$ case is a sign of potential flame instability. The higher consumption rate of the $100H_2\Omega$ case near the flame base region provides a thicker and shorter area compared to the $50H_2\Omega$ case, indicating possible stronger preferential diffusion effects. This preferential diffusion may lead to locally increasing H_2 consumption speed, involving a higher reactivity, and resulting in an upstream shift of the point of maximal reaction. This shorter and anchored flame front can potentially accelerate flashback formation [50].

Flame length

To quantify the shift observed for the diluted cases of the point where most of the reaction occurs, the characteristic flame length L_f is calculated as the distance between $z/D = -0.4$ (excluding the pilot flame and with D the diameter of the burner) and the stream-wise center of HRR intensity of the snapshot [51]:

$$L_f = \frac{\int z\,\overline{\dot{\omega}}_{T,xy}\,dz}{\int \overline{\dot{\omega}}_{T,xy}\,dz}, \tag{4}$$

with $\overline{\dot{\omega}}_{T,xy}$ the time-average of the HRR integrated along the axial direction z. The flame length of each case is reported in Fig. 4(b) by the white dashed line. The diluted conditions (except the $100H_2\Omega$ case), or reduced inlet temperature, clearly moving the point of reaction downstream, as shown by the slightly longer flame length of the $50H_2LT$, $50H_2\Omega$ and $50H_2EGR$ cases (with very similar lengths as the Ref case). Indeed, this spatial delay of the whole reactant oxidation (due to the inlet temperature reduction and/or diluted conditions) facilitates the flashback reduction by moving forward to the point where most of the reaction occurs. The wider reacting area of the $50H_2EGR$ case is confirmed by its longer flame length compared to the other cases, while the $100H_2\Omega$ case shows a shorter flame length close to the one shown by the FB case. This behavior was also assessed by the progress variable analysis from the hybrid 0D/1D calculations. On the contrary, the observed behavior of the $100H_2\Omega$ case tends towards the FB case.

Radial profiles

To extend these first observations and conclusions, a quantitative comparison is performed using the radial profiles of the time-averaged and fluctuating values of the temperature (Fig. 5(a) and (b)), and the

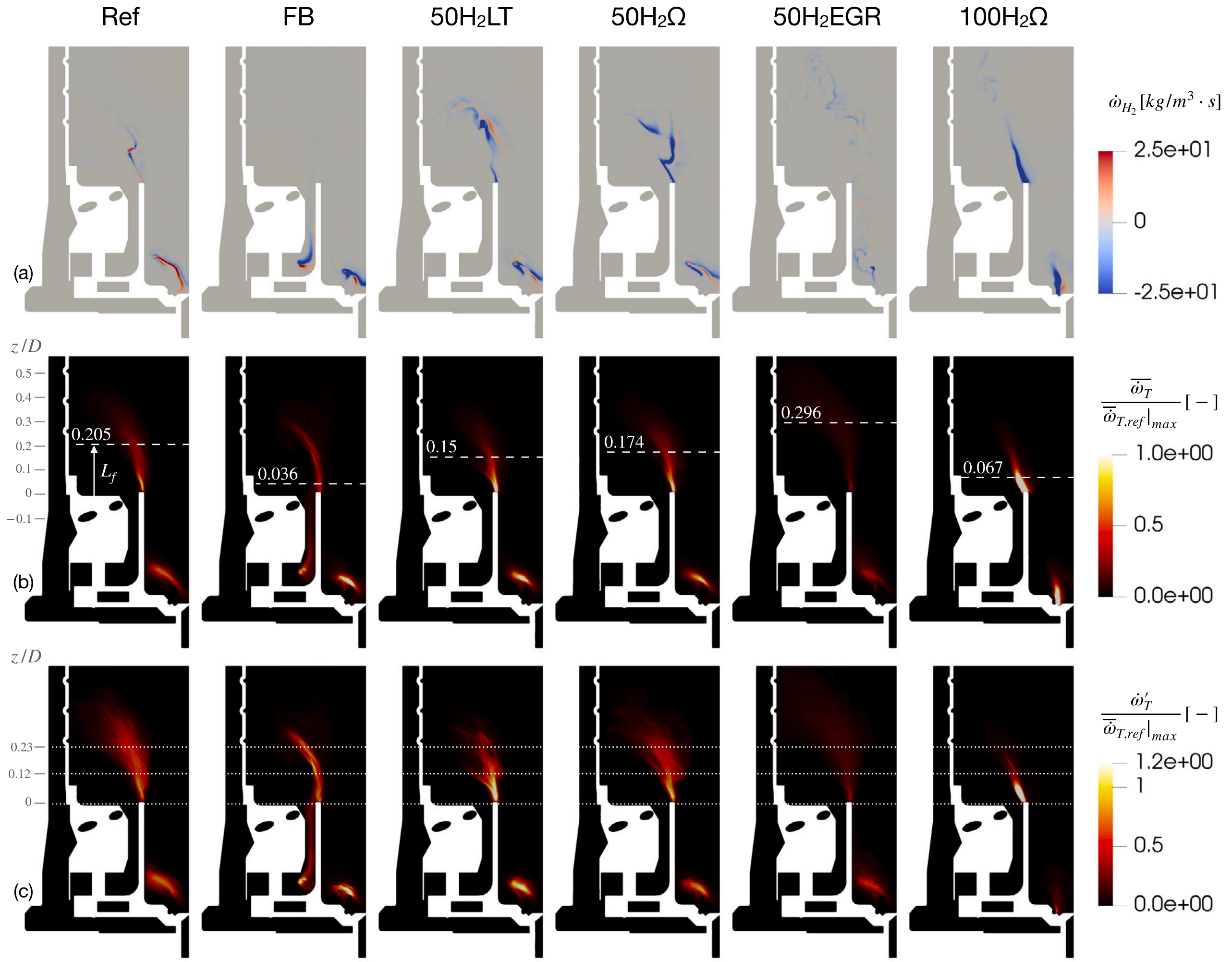

Fig. 4. The instantaneous H_2 source term $\dot{\omega}_{H_2}$ flow field distribution (a), the time-averaged (b) and fluctuating values (c) of the HRR $\dot{\omega}_T$ flow fields, both normalized by the maximal time-averaged HRR of the Ref case, show wider reacting region for the solution cases with a shift forward of the point where most of the reactions occur, except for the $100H_2\Omega$ case, as highlighted by the flame length position (reported in (b)).

ratio of the fluctuations over the time-averaged values of HRR $\dot{\omega}_T$ (Fig. 5(c)) at three different axial positions $z/D = 0\,/\,0.12\,/\,0.23$ (positions reported in Fig. 4(c)). In addition, the different regions of the burner from the center line to the burner walls are reported along the radial axis: the pilot flame from $r = 0R$ to $r = 0.38R$, the main swirling jet of the premixed flame from $r = 0.44R$ to $r = 0.59R$, and the ORZ from $r = 0.59R$ to $r = 1R$.

As first observation, it can be stated that the time-averaged temperature profiles are similar for all cases at the three specified positions (Fig. 5(a)). Nevertheless, three minor discrepancies can be highlighted. The first one is the slightly higher temperature level in $z/D = 0$ of the FB case at the radial level of the main jet resulting from flashback, whereas this profile tends to re-align with the other case profiles at $z/D = 0.12$. Then, the $100H_2\Omega$ case shows a higher temperature level at the same radial level (around $r = 0.44R$) in $z/D = 0.12$, compared to all the other cases. The third main difference, as already assessed, is the global lower temperature profiles of the $50H_2$EGR case at the three axial positions.

Regarding the temperature fluctuations in $z/D = 0$ (Fig. 5(b)), both the FB and, to a lesser extent, the $100H_2\Omega$ cases have more variations in the region of the main swirling jet (between $r = 0.44R$ and $0.59R$) than the other cases. However, all profiles become similar in $z/D = 0.12$, except the profile of the $100H_2\Omega$ case, which shows fewer fluctuations because of the homogeneous shorter flame on the whole injectors circumference. At $z/D = 0.23$, all profiles are similar.

Finally, when looking at the HRR ratio (Fig. 5(c)), the high level of fluctuations generated by the $100H_2\Omega$ case at the flame base ($z/D = 0$), compared to the other cases, is an additional sign of risk of flame instability. Indeed, the HRR variations of this case shows a peak reaching almost 8 times the values reached by the time-averaged HRR in the main jet region, and this case still has the highest fluctuations in both other radial regions (pilot flow region and ORZ region). Next to this case, there is the FB case that presents slightly lower fluctuations than the $100H_2\Omega$ case in the main jet region, with almost a HRR ratio of 5.5, and similar profiles than the other cases in both pilot flow and ORZ positions. For both $z/D = 0.12$ and $z/D = 0.23$ positions, the $100H_2\Omega$ case has the lowest variations of HRR compared to the other cases, potentially because of the higher reacting and shorter flame leading to the early consumption of the reactants. In these positions, we can see the flow interaction between the ORZ and the main swirling jet for the other cases, with a peak of reaction in the shear layer of these flows, ensuring the good mixing of the species and the flame stabilization, as also experimentally observed in a similar configuration by [52].

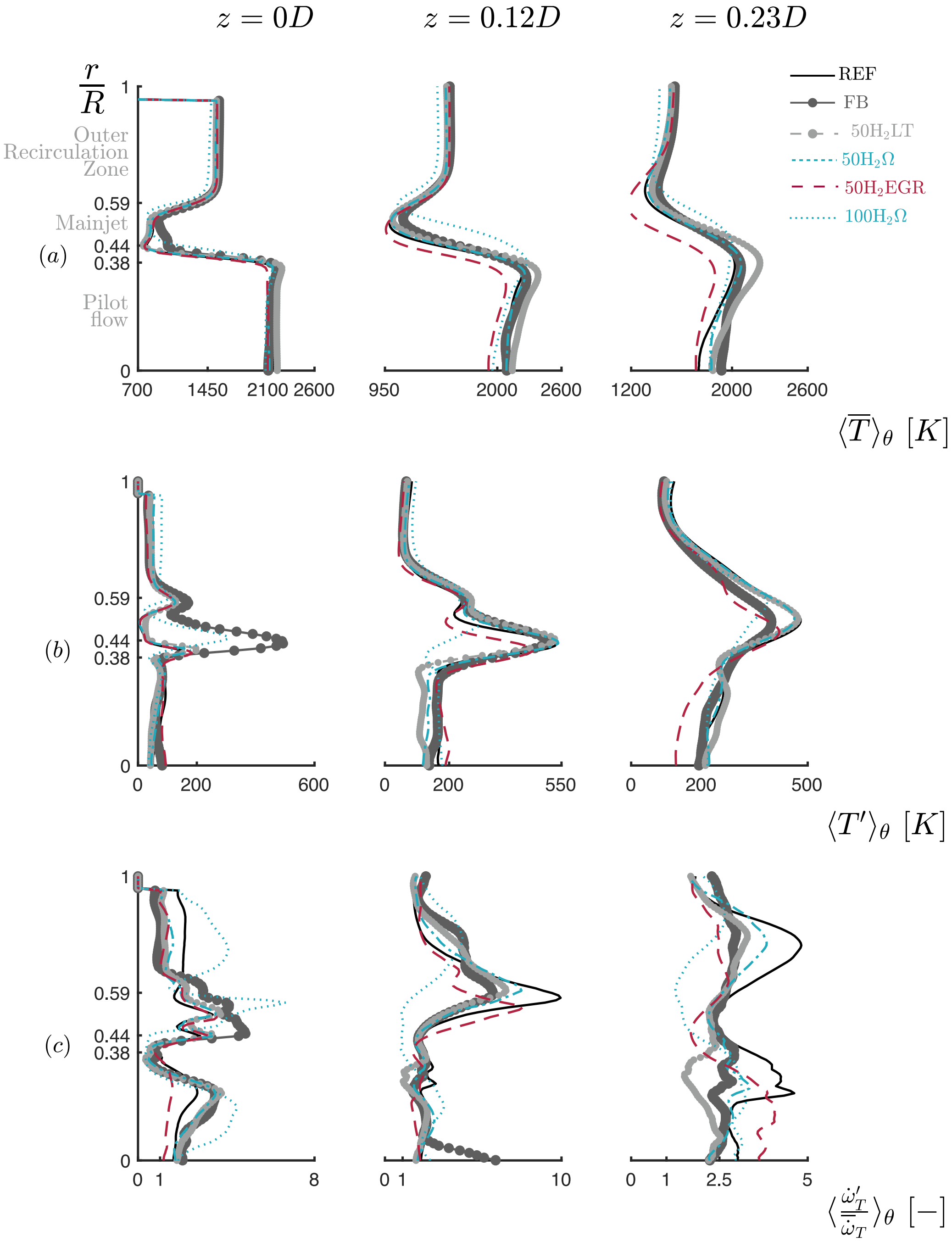

Fig. 5. Azimuth means of the radial profiles in three different axial position $z/D = 0\,/\,0.12\,/\,0.23$ showing the time-averaged temperature (a), the temperature fluctuations with the RMS values (b), and the ratio of the fluctuations over the time-averaged of the heat release rate $\dot{\omega}_T$, showing that the $50H_2\Omega$ case is the closest to the Ref case in terms of performances.

4.4. Flame stability

In this part, the LES results are used for a stability analysis of the different cases. Although the mechanisms leading to instability are numerous, and still difficult to predict with a reliable method, especially when acoustic waves are not simulated, some insights may be gained by identifying some characteristics of instability.

Combustion regime

Since the main flame of the studied burner is premixed, a turbulent regime diagram is first drawn to learn more about the combustion regime, as proposed by Peters [53]. In this diagram, the turbulent flame is characterized by the turbulent velocity u' and turbulent length scale l_t used with laminar flame characteristics, such as the unstretched laminar flame speed S_l^0 and the diffusive thickness δ (as defined in Eq. (2)) [40]. The turbulent velocity u' is defined by the Root Mean Square (RMS) velocities in the three spatial directions:

$$u' = \left(\frac{u_x'^2 + u_y'^2 + u_z'^2}{3} \right)^{\frac{1}{2}}, \tag{5}$$

and the turbulent length scale l_t is calculated using the turbulent velocity u' and the viscous dissipation rate ϵ:

$$l_t = \frac{u'^3}{\epsilon}, \tag{6}$$

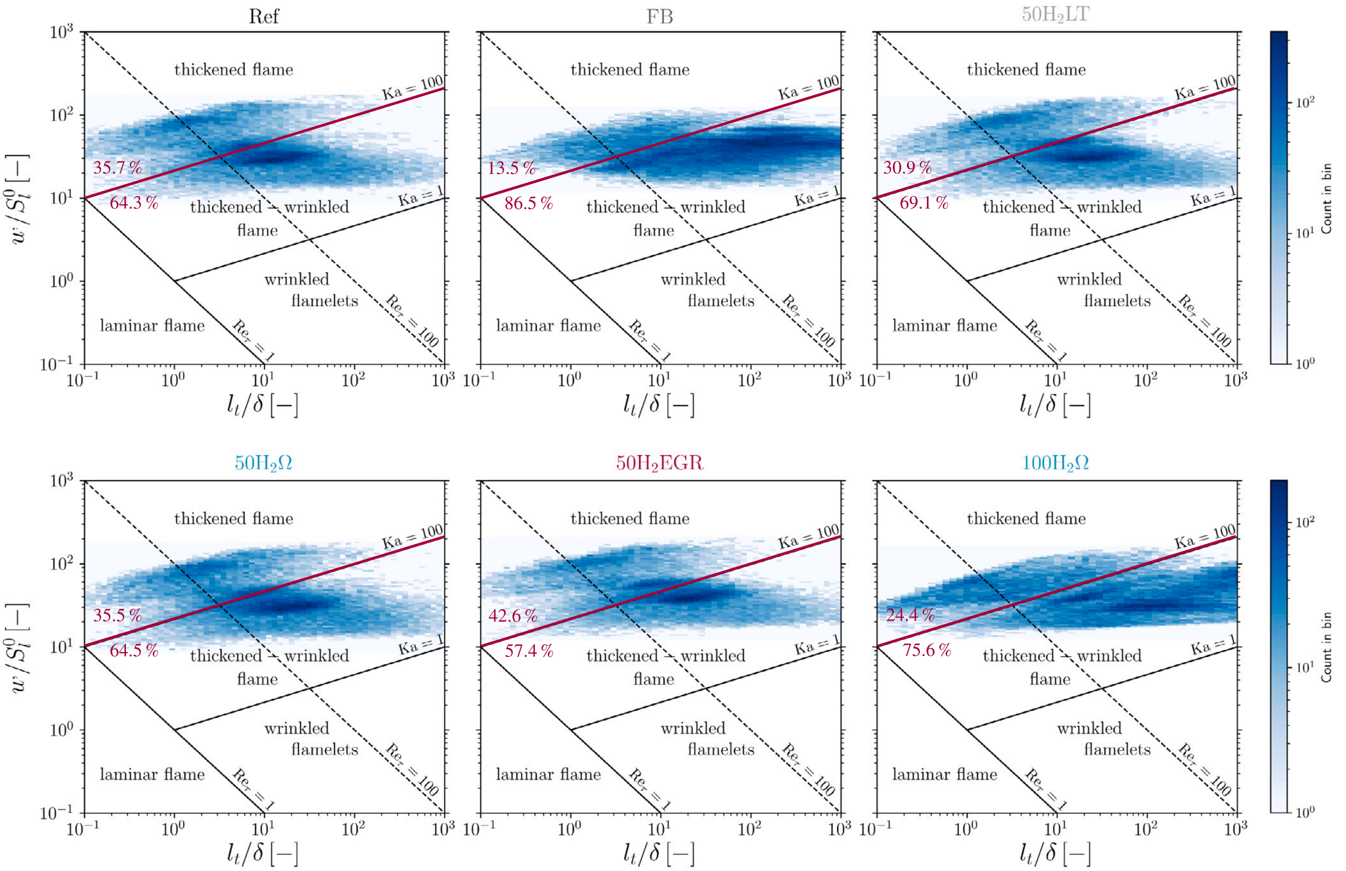

Fig. 6. Combustion regime diagram comparison between all the simulated cases using scatter plots of the ratio u'/S_L^0 in function of the ratio l_t/δ. For all cases, the combustion regime is mainly the thickened-wrinkled flame. To quantify the point distribution, the percentage of points above and below Ka = 100 are highlighted in red.

$$\epsilon = 2\nu S_{ij} S_{ij}, \tag{7}$$

with ν the kinematic viscosity and S_{ij} the fluctuating strain rate. Finally, the different region of the diagram are separated by the Karlovitz number, defined as follow:

$$Ka = \left(\frac{l_t}{\delta}\right)^{-1/2} \left(\frac{u'}{S_l^0}\right)^{3/2} \tag{8}$$

Fig. 6 shows the scatter plots with a density map of the fresh gases before the flame, to compare the turbulent regime diagrams of all cases [54], from white to dark blue to count the number of point. The aim of this distribution comparison is to highlight similarities or discrepancies. Indeed, the obtained point distributions are sensitive to the way of computing the physical quantities l_t/δ and u'/S_L^0, giving thus only major trends. To build the results shown in Fig. 6, the region of the fresh gases in the main swirler and injectors before the main flame has been manually defined to select the points of the domain considered for the calculation of the required dimensionless numbers.

For all cases, most of the points are found between the lines defined by the Karlovitz numbers Ka = 1 and Ka = 100, i.e. in the so-called *thickened-wrinkled flame* regime [40]. In this combustion regime, the turbulent vortices can enter, thicken and modify the flame preheat zone, but not the reaction zone, which is only wrinkled. Moreover, we can observe that a not negligible fraction of points are located above the Ka = 100 line. Most of these points located above Ka = 100 are a result of the contribution of the dynamics of the second swirler. As explained, this swirler (injecting only the oxidizer) is used to enhance the tangential momentum of the main injectors for flame stabilization. To quantify the point distribution, the percentage of points above and below Ka = 100 are highlighted in red in Fig. 6, pointing out the contribution of the second swirler on the combustion regime. For *thickened flames* (Ka > 100), both diffusion and reaction zone are affected by turbulent motions, and laminar structure could no longer be identified. In addition, most of the points are found above the turbulent Reynolds number line of $\mathrm{Re}_\tau = 100$, corresponding to moderate to significant turbulence near the flame.

The diagram matching best the Ref case (Fig. 6), showing almost the same point distributions, is the 50H$_2\Omega$ case, followed by the 50H$_2$LT case, and the 50H$_2$EGR case, which shows however more points in the *thickened flame* regime (42.6% compared to 35.7% in the Ref case). Among the solution cases, the farthest from the Ref case is the 100H$_2\Omega$ case. With 24.4% of points in the *thickened flame* regime, the point distribution of this case is closer to the 13.5% of the FB case compared to the 35.7% of the Ref case. This reduced amount of points in the FB case in the *thickened flame* regime comes from the lower amount of fresh gases available for the main injectors due to flashback.

Flame topology

The flame topology, the vorticity and turbulence interaction of the solution cases are compared to the Ref and FB cases in Figs. 7 and 8. In Fig. 7, using 3D instantaneous iso-contours of the flame sensor of the TFLES model (from an iso-value of the defined progress variable), the flame front shape is colored by the temperature (left-hand side contour), and the instantaneous iso-contour of the Q-criterion (at $8 \cdot 10^{-8}$ s^{-2}), highlighting the resolved turbulent structures [55], is colored by the u'/S_L^0 ratio (right-hand side contour). In Fig. 8, the normalized vorticity is shown using a grayscale color, highlighted using a red flame front contour (iso-line defined by the 3D contour printed on the slice).

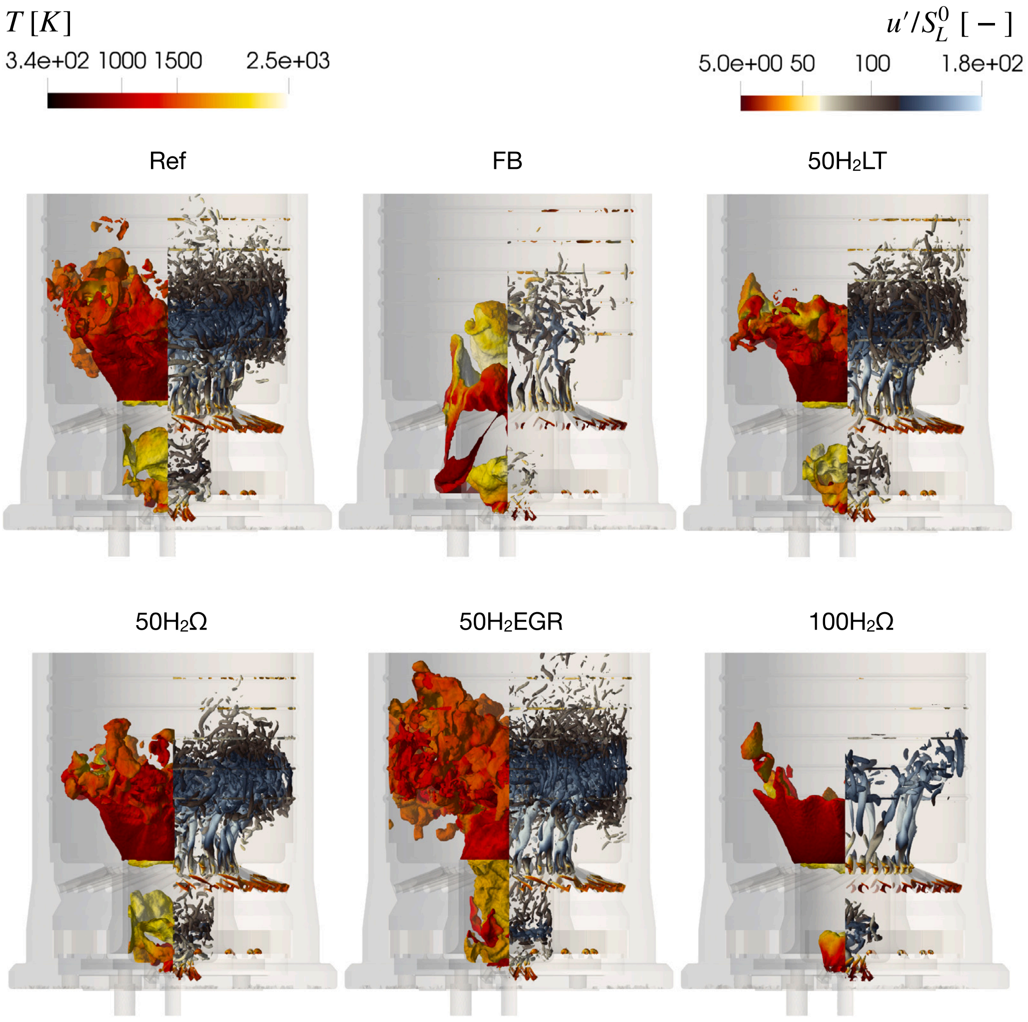

Fig. 7. Flame topology comparison between the Ref case, the FB case and the solution cases. The left-hand side contours shows the 3D instantaneous iso-contours of the flame sensor of the TFLES model (from an iso-value of the defined progress variable), highlighting the flame front shape, colored by the temperature, and the right-hand side shows the instantaneous iso-contour of the Q-criterion (at $8 \cdot 10^8$ s^{-2}), colored by the u'/S_L^0 ratio. As the Ref case, the solution cases present an anchored flame base conjugated to the turbulence shaping the flame front.

The presented results show that the diluted and lower inlet temperature conditions allow limiting the flashback apparition by either spreading the burning area or reducing the HRR or the H_2 consumption local concentration. The main observed characteristics on the flame/turbulence interaction are for all cases: an anchored flame base to the outer section of the main injectors; a higher temperature located in the inner surface of the flame coming from the hotter pilot gases; an ORZ flame stabilization mechanism (by reducing the axial momentum and belting the flame base) conjugated with an increased small-scaled turbulence in and out of the flame top and high u'/S_L^0 ratio; and a more upstream anchor point observed for the 100$H_2\Omega$ case with a lower u'/S_L^0 ratio near the flame base.

All cases present a flame base anchored to the outer section of the main injectors, showing a global V-shape flame topology. For all cases, the inner flame envelope attached to the main injectors shows higher temperature values compared to the outer one. This anchoring zone of the flame envelope stresses the stabilizing effect of the ORZ near the flame base on the combustion process. Then, we can also observe that the 50H_2LT and 50$H_2\Omega$ cases show the flame shape and Q-criterion distribution the closest to the Ref case. In addition, all cases globally present a strong vorticity near the flame base shaping the external envelope of the flame due to the ORZ. Nevertheless, contrary to the 100$H_2\Omega$ and FB cases, the other cases show small-scale vortices surrounding and penetrating the top of the flame, conditioning its more wrinkled shape. This difference with the 100$H_2\Omega$ case was already presumed when comparing the combustion regime diagrams. Indeed, these observed penetrating vortices are due to the contribution of the 30% of points in the *thickened flame* regime of the Ref, 50H_2LT, 50$H_2\Omega$ and 50H_2EGR diagrams, in which both diffusion and reaction zone are affected by turbulent motions. Another difference of the 100$H_2\Omega$ and FB cases is the lower u'/S_L^0 ratio near the flame base (already observed with the combustion regime diagram Fig. 6), down to around u'/S_L^0 ∼50 while the other cases show a range from 100 to 150, justifying the observed smaller penetration of the turbulence in the flame. On the other hand, Fig. 8 shows less small turbulence structure for these two cases. The shorter and highly reactive flame observed in both cases is limiting the interaction between turbulence and the flame tip.

Finally, the 50H_2EGR case shows a wider flame, expanding more downstream compared to the other case. In addition, a less continuous flame shape near the flame base can be observed, and a more wrinkled top flame, which may lead to a less stable and well-attached flame. This converges with the previous observations for this case. Nevertheless, the high level of vortices entering and shaping the flame has to be correlated to the higher percentage of points in the *thickened flame*

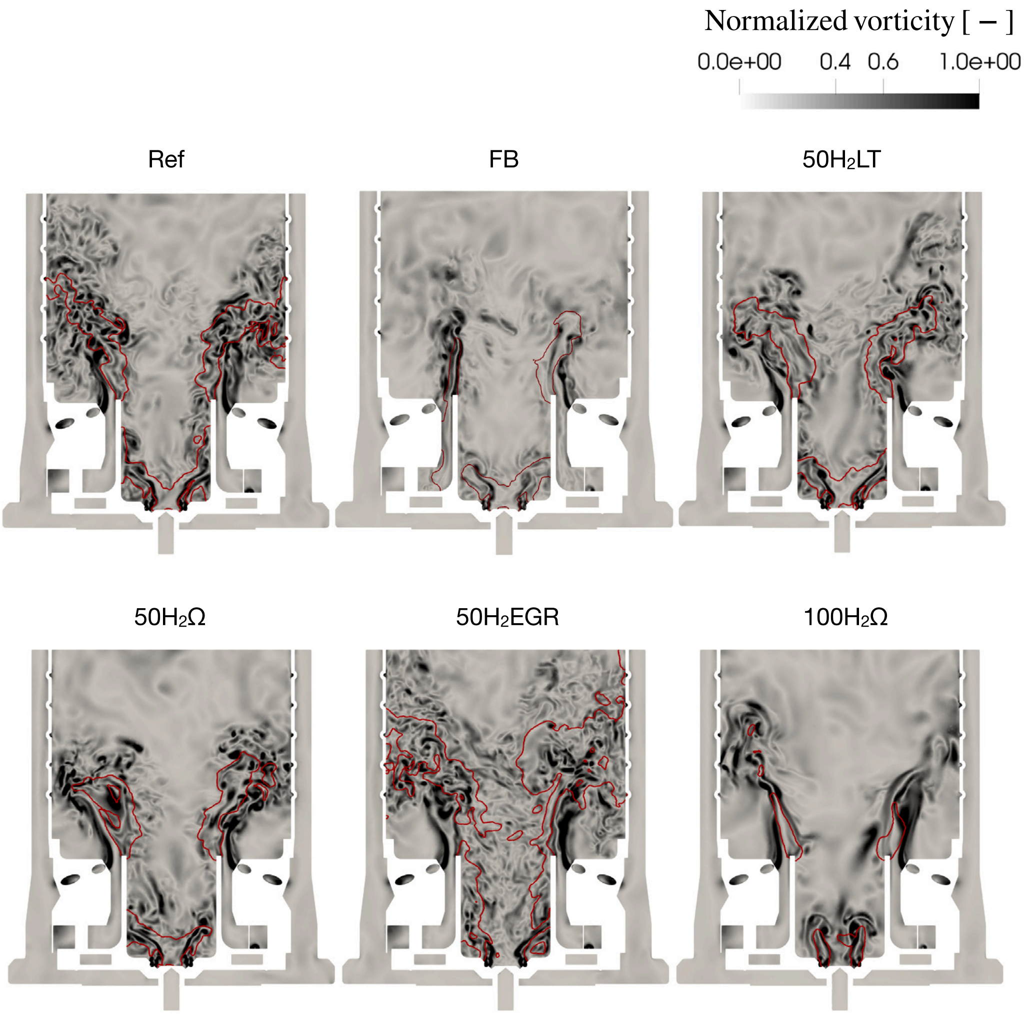

Fig. 8. Flame/turbulence interaction comparison between the Ref case, the FB case and the solution cases is shown using the instantaneous normalized vorticity, with the flame front footprint highlighted using a red contour. The turbulence is highly shaping the flame tip of the 50H_2EGR case.

regime observed in Fig. 6 compared to the other cases, with almost 43% of the points for the 50H_2EGR case.

Frequency analysis

After analyzing the impact of the dilution on the turbulent structure interaction with the flame front, a frequency analysis is performed. Fig. 9 shows the Power Spectral Density using a Welch method [56] of the axial velocity for an arbitrary point in the shear layer between the Inner Recirculation Zone (IRZ) and Outer Recirculation Zone (ORZ) of the main flame. First, a global signal decrease with frequency is observed for all cases. This global decrease is expected due to the inertial spectrum being dominated by turbulence. Then, the Ref case shows a clear peak between 3 and 4 kHz. The only case that reproduces this peak is the 50$H_2\Omega$ case, while the other cases show no dominant frequency. This frequency, between 3 and 4 kHz, corresponds to instabilities/fluctuations of turbulent smaller-scales, and indicates that the measurement location lies within the vortex breakdown region generated by the swirling flow. Indeed, the probe is positioned in the shear layer between the IRZ and ORZ of the main swirling flame. The vortex breakdown location is thus not the same for the Ref and 50$H_2\Omega$ cases as the other cases. In contrast to the other solution cases, this similar mode could be explained by the lower dilution level of the 50$H_2\Omega$ case compared to the 50H_2EGR and 100$H_2\Omega$ cases. However, although no dilution is performed for the 50H_2LT case, no dominant frequency can be distinguished either. Therefore, in this study, we cannot state that the dominant mode of the Ref case is suppressed by diluted conditions.

4.5. Local flame states comparison

To analyze the flame dynamics locally in the solution cases, the domain volumes near the main premixed flame of all cases were axially sampled into sub-volumes along the streamwise direction to obtain statistically converged quantities, as done in [57]. Then, the time-averaged turbulent flame speeds S_T and surface areas A_T were computed for each sub-volume, and their normalized streamwise evolutions are shown in Fig. 10. Several definitions of turbulent flame speed are available in the literature. In this study, the turbulent flame speed is defined as a turbulent consumption speed based on the reaction rate of the fuel mass fraction $\dot{\omega}_F$:

$$S_T = -\frac{1}{\rho Y_F A_T^0} \int_V \dot{\omega}_F \, dV, \tag{9}$$

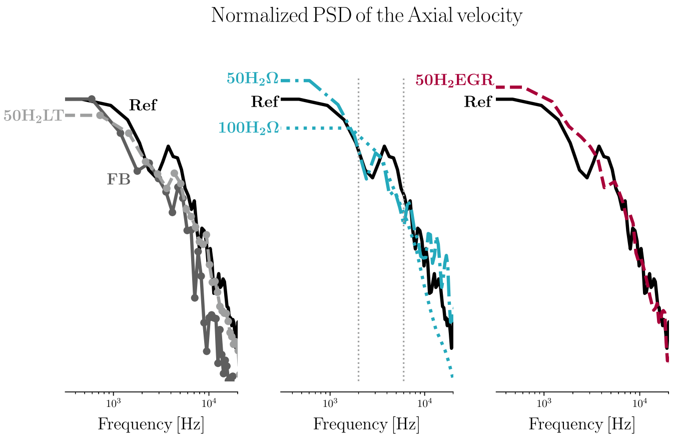

Fig. 9. The normalized PSD of the axial velocity for an arbitrary point in the shear layer between the IRZ and ORZ of the main flame shows for the Ref case one distinguishable mode between 3-4kHz, only reproduced by the 50H$_2\Omega$ case.

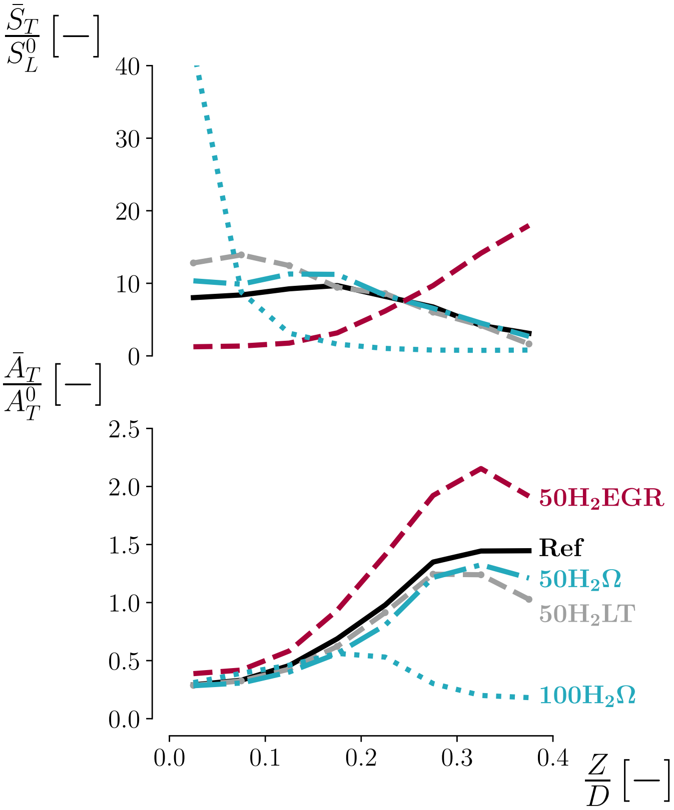

Fig. 10. Streamwise evolution of S_T/S_L^0 and A_T/A_T^0 showing that the 50H$_2$LT and the 50H$_2\Omega$ cases behave similarly to the Ref case, while the 50H$_2$EGR case presents a rising turbulent flame speed S_T along with an increasing flame surface from foot to top. On the contrary, the 100H$_2\Omega$ reaches a 4 times higher S_T than the Ref case at the flame foot before dropping down.

with ρ the unburnt gas density, Y_F the fuel mass fraction in the unburnt mixture, and A_0 is a reference surface, selected equal to the time-averaged flame area of the Ref case $A_T^0 = \langle \bar{A}_{T,ref} \rangle$ for this work. The turbulent flame surface is created and calculated from the iso-surface defined by the flame sensor of the TFLES model at an iso-value $S = 0.5$. As explained in the numerical setup section, this flame sensor is defined based on a progress variable and set to a value that provides the most reactive iso-surface.

The turbulent flame speed $\bar{S}_T$ and flame area A_T evolutions along the streamwise direction of the 50H$_2$LT and 50H$_2\Omega$ cases are very similar to those of the Ref case (Fig. 10). For these three cases, the turbulent flame speed initially remains nearly constant in the first region of the flame before dropping, while the 50H$_2$EGR case and 100H$_2\Omega$ case show opposite behaviors. The large increase in turbulent flame speed for the 50H$_2$EGR case is induced by flame-flame interaction, as similarly observed by [58], and linked to the increase in flame surface. In all cases, flame surfaces expand in the initial flame regions before being destroyed by mechanisms described by Rieth et al. [59]. The higher turbulent intensity near the flame base (as previously observed) leads to lower turbulent advection time scales (related to flame surface

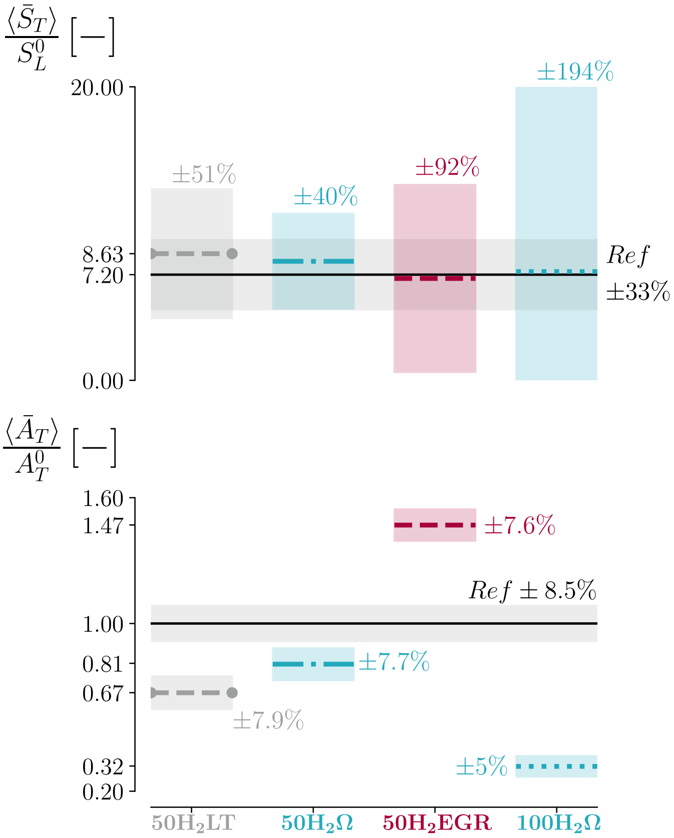

Fig. 11. The time- and space-averaged flame speeds $\langle \bar{S}_T \rangle$ and surfaces $\langle \bar{A}_T \rangle$ of the different solution cases are compared, where the mean values are highlighted along with the fluctuations represented by the box width. The turbulent flame speeds of the solution cases are very close to the one of the Ref case, positively encouraging the choice of the laminar flame speed as a criterion for flashback limitation.

destruction) than molecular time scales (related to diffusive transport), resulting in higher Karlovitz numbers, as described by Rieth et al. [59]. Therefore, locally A_T decreases more in cases with the most significant drop in S_T/S_L^0. Consequently, the deviation of S_T from S_L^0 arises from intense HRR, which in the $100H_2\Omega$ case can even disrupt H_2 diffusive fluxes [60]. The transition between turbulent flame and surface area contributions occurs farther upstream than in other cases due to more intense burning in the early region.

The hydrogen and diluted conditions impact on the flame stability is also analyzed through the time-and space-averaged turbulent flame speed $\langle \bar{S}_T \rangle$ and surface $\langle \bar{A}_T \rangle$ respectively normalized by the laminar flame speed of the related case and by the time- and space-averaged turbulent flame surface of the Ref case $A_T^0 = \langle \bar{A}_{T,ref} \rangle$. In Fig. 11, the mean values of the solution cases are highlighted along with the fluctuations represented by the boxes width. Regarding the turbulent flame speeds, the obtained results are interesting and encourage the choice of the laminar flame speed as the selected criterion for the hybrid 0D/1D model to obtain the diluted conditions to limit flashback. Indeed, all cases present similar average values to the Ref case, and are kept in the range of fluctuations observed for the Ref case. This means that the educated guess of the dilution level or temperature decrease from our 0D/1D model is accurate enough to bring the turbulent flame speed of hydrogen (or hydrogen blend) combustion very close to the same levels of pure methane combustion.

Although this criterion may not be precise enough for all cases to exactly match the fluctuations or the turbulent flame surface evolution of the Ref case, it still provides an additional clue about whether conditions are approaching the edges of stability or flashback disruption. The fluctuation levels of the $50H_2LT$ case and $50H_2\Omega$ case are slightly higher than those of the Ref case, while the increasing fluctuation in the turbulent flame speed of the $50H_2EGR$ case and $100H_2\Omega$ case should be linked to the results on the turbulent flame area. The primary reason lies in the different dilution methods and mechanisms, as previously observed and described. While the $50H_2EGR$ case exhibits the largest flame surface (due to high dilution) and the $100H_2\Omega$ the smallest (because of stronger reactions and higher turbulence), the fluctuation levels of flame area across all cases remain similar to those of the Ref case (less than 1% difference for the cases $50H_2LT$, $50H_2\Omega$ and $50H_2EGR$). The higher fluctuation level of turbulent flame speed in the $50H_2EGR$ case, combined with larger flame surface, could lead to blow-off issues. Conversely, the $100H_2\Omega$ case shows the smallest surface area and the lowest fluctuation level, at only 5%. Moreover, the higher fluctuation level of the turbulence level observed for the $100H_2\Omega$ case comes from the large variation of its turbulent flame speed from base to top flame (from $S_T/S_L^0 = 40$ to 0 over $Z/D = 0$ to $Z/D = 0.15$, as shown in Fig. 10), in opposition of the observed behavior for the other cases, because of the higher reactivity of this case as shown through different analysis. This turbulent flame behavior, along with the highest fluctuation in turbulent flame speed, indicates that the $100H_2\Omega$ case is approaching conditions close to flashback, even though flashback was not observed.

4.6. Practical considerations

In this section, the LES results are discussed and compared to the predictions obtained in [22] to bring some criticism on the 0D/1D model. Among all the cases presented to prevent flashback, none show increases in temperature, peak HRR, or flame front propagation in the main premixed injectors. This gives a first initial validation of the proposed fast prediction method using the hybrid 0D/1D model described in [22]. Nevertheless, the LES results reveal two distinct behaviors for the $100H_2\Omega$ and $50H_2EGR$ cases, which the 0D/1D model cannot predict due to its limitations in capturing flame dynamics or turbulence interactions.

Although the $100H_2\Omega$ case does not show any sign of flashback, the observed flame shape and results suggest that this case may be more sensitive to developing upstream flame propagation through the injectors. This case exhibits a shorter flame with a more intense HRR, a thicker consumption rate area, higher HRR levels, and turbulent flame speed fluctuations over time near the flame base. Its combustion regime is closer to the FB case than to the other cases. Conversely, the wider and thinner HRR front, combined with the wider and less structured consumption rate area shown by the $50H_2EGR$ case, could potentially compromise the integrity of a well-attached and stable flame, even though this case appears to be free of any flashback risk.

The statement of validation of the predetermined conditions from 0D/1D must be nuanced by considering some practical constraints related to actual mGT facilities. First, the *Progress allowance* Pa number introduced in this study and the LES results can help in defining the limit of acceptable conditions to avoid flashback. Indeed, the results for the $50H_2EGR$ cases show that the predictions from [22] may appear as too conservative with $Pa = 8.84$, almost twice the value for the Ref case. However, a security margin has to be taken into account on the predetermined optimized levels of dilution to avoid any facility issues, especially when looking at the results for the $100H_2\Omega$ case, which present a similar Pa number than the Ref case. In an actual burner, the heat transfer between the flame and the burner walls will increase the wall temperature which might become a source of energy triggering flashback. In addition, we showed that the temperature is a key parameter in controlling flashback, but the need for temperature reduction is a major drawback on the mGT cycle performances. Therefore, the methodology proposed in [22] provides a fast model capable of delivering reasonable predictions for flashback prevention, but the stability criterion must be adjusted based on the obtained LES results and the defined *Progress allowance* number (with a threshold defined at $Pa = 2$, as previously explained). These insights, combined with a thermodynamic analysis to ensure cycle performances, might serve as a perspective basis for future works.

5. Conclusion

Aiming at stabilizing and restricting flashback in an actual mGT (Turbec T100) fueled by hydrogen blends without any redesign of the combustor, this work presented a verification of the potential of humidification and EGR, as well as the predicted dilution levels provided by our previously presented 0D/1D model, in preventing flashback. To do so, Large-Eddy Simulations (LES) of an original mGT combustor layout, using a complex chemistry approach with an Adaptive Mesh Refinement methodology, were performed to compare pure methane combustion, considered as a reference case, to a case with a CH_4/H_2 blend of $50/50\%_{vol}$, highlighting flashback, and to cases with a solution to limit this flashback (humidification and EGR) for different hydrogen fractions, 50% and 100%.

The numerical results show that flashback is avoided in all considered solution cases, confirming that the chosen criterion — namely, the laminar flame speed — is effective in estimating operating conditions to prevent flashback. It appears that the $50H_2\Omega$ case provides, through the different analyses, presents the closest behavior to the Ref case, followed by the $50H_2LT$. Indeed, the $50H_2EGR$ case presents a wider and thinner HRR front, potentially leading to a more unstable flame base compared to the other cases, even though this case seems free of any flashback risk. Although the 100% $H_2\Omega$ case does not show any sign of flashback, neither the observed shorter flame shape and obtained results, showing some similarities with the FB case, suggest that this case may be more sensitive to develop an upstream flame propagation through the injectors. In addition, despite the 4 times higher turbulent flame speed observed at the flame foot of the $100H_2\Omega$ case, the average turbulent flame speed remains rather constant for all cases. Therefore, the obtained results confirm that the proposed approach works for moderate H_2 levels, but requires further investigation for full hydrogen.

Finally, this work first ambition was to sufficiently prove through high-fidelity simulations the functionality of humidification and EGR in avoiding flashback. The natural next step will feature a validation of this proposed approach on an experimental test rig. Another perspective would be to perform an optimization analysis for both the dilution levels for the flame stability and for the cycle performances in terms of efficiency and produced power. Indeed, the results show that the most impacting parameter is the temperature. Nevertheless, a lower temperature would negatively impact the cycle performances, while humidified conditions would help maintaining or increasing the gas turbine cycle performances.

CRediT authorship contribution statement

Alessio Pappa: Writing – original draft, Methodology, Investigation, Formal analysis, Data curation, Conceptualization. **Laurent Bricteux:** Writing – original draft, Supervision, Conceptualization. **Ward De Paepe:** Writing – original draft, Supervision, Conceptualization.

Declaration of competing interest

The authors declare that they have no known competing financial interests or personal relationships that could have appeared to influence the work reported in this paper.

Acknowledgments

The present research benefited from computational resources made available on Lucia, the Tier-1 supercomputer of the Walloon Region, infrastructure funded by the Walloon Region under the grant agreement n°1910247. The authors thank also G. Lartigue and V. Moureau for providing the code YALES2. Alessio Pappa acknowledges, as Postdoctoral Researcher, the support of the Fonds de la Recherche Scientifique de Belgique (F.R.S.-FNRS) [CR 40024661], and for the financial support from the Hydrogenate project (T004222F; Funder ID:10.13039/501100002661).

Appendix A. Supplementary data

Supplementary material related to this article can be found online at https://doi.org/10.1016/j.jaecs.2026.100482.

Data availability

Data will be made available on request.

References

[1] Odenweller A, Ueckerdt F. The green hydrogen ambition and implementation gap. Nat Energy 2025;10(1):110–23, Publisher: Nature Publishing Group.

[2] Genovese M, Schlüter A, Scionti E, Piraino F, Corigliano O, Fragiacomo P. Power-to-hydrogen and hydrogen-to-x energy systems for the industry of the future in Europe. Int J Hydrog Energy 2023;48(44):16545–68.

[3] Taamallah S, Vogiatzaki K, Alzahrani F, Mokheimer E, Habib M, Ghoniem A. Fuel flexibility, stability and emissions in premixed hydrogen-rich gas turbine combustion: Technology, fundamentals, and numerical simulations. Applied Energy 2015;154:1020–47.

[4] Funke HH-W, Beckmann N, Keinz J, Horikawa A. 30 years of dry-low-NOx micromix combustor research for hydrogen-rich fuels—An overview of past and present activities. J Eng Gas Turbines Power 2021;143(7).

[5] McClure J, Abott D, Agarwal P, Sun X, Babazzi G, Sethi V, Gauthier PQ. Comparison of hydrogen micromix flame transfer functions determined using RANS and LES. In: ASME turbo expo 2019: GT2019-90229. 2019.

[6] Magnusson R, Andersson M. Operation of SGT-600 (24 MW) DLE gas turbine with over 60% H2 in natural gas. In: ASME turbo expo 2020: GT2020-16332. 2020.

[7] Bothien MR, Ciani A, Wood JP, Fruechtel G. Sequential combustion in gas turbines: The key technology for burning high hydrogen contents with low emissions. In: ASME turbo expo 2019: 19-90798. 2019.

[8] Thielens V, Demeyer F, De Paepe W. Experimental investigation of CH4/H2 blends on the emissions of a micro gas turbine setup with enhanced exhaust gas recirculation. In: 1st belgian symposium of thermodynamics, carnot. 2024, p. 46(1–5).

[9] Banihabib R, Lingstädt T, Wersland M, Kutne P, Assadi M. Development and testing of a 100 kw fuel-flexible micro gas turbine running on 100% hydrogen. Int J Hydrog Energy 2024;49:92–111.

[10] Wunning JA, Wunning JG. Flameless oxidation to reduce thermal no-formation. Prog Energy Combust Sci 1997;23:081702–081702–9.

[11] Zornek T, Monz T, Aigner M. Performance analysis of the micro gas turbine turbec T100 with a new FLOX-combustion system for low calorific fuels. Appl Energy 2015;159:276–84.

[12] Goke S, Furi M, Bourque G, Bobusch B, Gockeler K, Kruger O, Schimek S, Terhaar S, Paschereit CO. Influence of steam dilution on the combustion of natural gas and hydrogen in premixed and rich-quench-lean combustors. Fuel Process Technology 2013;107:14–22.

[13] Krüger O, Terhaar S, Paschereit CO, Duwig C. Large Eddy Simulations of Hydrogen Oxidation at Ultra-Wet Conditions in a Model Gas Turbine Combustor Applying Detailed Chemistry. J Eng Gas Turbines Power 2013;135(021501).

[14] Pappa A, Cordier M, Bénard P, Bricteux L, De Paepe W. How do water and CO2 impact the stability and emissions of the combustion in a micro gas turbine? — A large eddy simulations comparison. Energy 2022;248:123446.

[15] Palulli R, Zhang K, Dybe S, Yasir M, Paschereit CO, Duwig C. Investigation of NO formation in non-premixed, swirl-stabilised, wet hydrogen/air gas turbine combustor. Fuel 2024;378:132943.

[16] du Toit M, Engelbrecht N, Oelofse SP, Bessarabov D. Performance evaluation and emissions reduction of a micro gas turbine via the co-combustion of H2/CH4/CO2 fuel blends. Sustain Energy Technol Assessments 2020;39:100718.

[17] Hasti VR, Lucht RP, Gore JP. Large eddy simulation of hydrogen piloted CH4/air premixed combustion with CO2 dilution. J the Energy Inst 2020;93(3):1099–109.

[18] Stathopoulos P, Kuhn P, Wendler J, Tanneberger T, Terhaar S, Paschereit CO, Schmalhofer C, Griebel P, Aigner M. Emissions of a Wet Premixed Flame of Natural Gas and a Mixture With Hydrogen at High Pressure. J Eng Gas Turbines Power 2016;139(041507).

[19] De Paepe W, Sayad P, Bram S, Klingmann J, Contino F. Experimental Investigation of the Effect of Steam Dilution on the Combustion of Methane for Humidified Micro Gas Turbine Applications. Combust Sci Technol 2016;188(8):1199–219.

[20] Verhaeghe A, Dubois L, Bricteux L, Thomas D, Blondeau J, De Paepe W. Carbon capture performance assessment applied to combined cycle gas turbine under part-load operation. J Eng Gas Turbines Power 2022;145(4):041009.

[21] Pousada PR, Doan NAK, Aditya K, Düsing M, Ciani A, Langella I. Flashback Prevention in a Hydrogen-Fueled Reheat Combustor by Water Injection Optimized With Global Sensitivity Analysis. J Eng Gas Turbines Power 2025;147(6):061021.

[22] Pappa A, Bricteux L, De Paepe W. A strategy based on hybrid 0D chemical reactor networks and 1D flame predictions for flashback prevention in an original H2 fueled micro gas turbine combustor without any redesign. Int J Hydrog Energy 2025;111:264–77.

[23] Turbec. T100 microturbine CHP system: Technical description version 4.0. 2010-2011.

[24] Tuncer O, Acharya S, Uhm J. Dynamics, NOx and flashback characteristics of confined premixed hydrogen-enriched methane flames. Int J Hydrog Energy 2009;34(1):496–506.

[25] Moureau V, Domingo P, Vervisch L. Design of a massively parallel CFD code for complex geometries. Comptes Rendus Mec 2011;339(2-3):141–8.

[26] Chorin AJ. Numerical solution of the Navier-Stokes equations. Math Comp 1968;22:745–62.

[27] Pierce CD, Moin P. Progress-variable approach for large-eddy simulation of non-premixed turbulent combustion. 2004;504:73–97.

[28] Kraushaar M. Application of the compressible and low-mach number approaches to large-eddy simulation of turbulent flows inaero-engines (Ph.D. thesis), CERFACS; 2011.

[29] Bénard P, Moureau V, Latrigue G, D'Angelo Y. Large-eddy simulation of a hydrogen enriched methane/air meso-scale combustor. Int J Hydrog Energy 2011;42(4):2397–410.

[30] Boulet L, Bénard P, Lartigue G, Moureau V, Didorally S, Chauvet N, Duchaine F. Modeling of conjugate heat transfer in a kerosene/air spray flame used for aeronautical fire resistance tests. Flow, Turbul Combustion 2018;101(2):579–602.

[31] Bénard P, Lartigue G, Moureau V, Mercier R. Large-eddy simulation of the lean-premixed preccinsta burner with wall heat loss. Proc. Inst. 2019;37(4):5233–43.

[32] Germano M, Piomelli U, Moin P, Cabot W. A dynamic subgrid-scale eddy viscosity model. Phys Fluids 1991;3(7):1760–5.

[33] Hirschfelder JO, Curtiss CF, Bird RB. Molecular theory of gases and liquids. John Wiley & Sons, New-York 1954;17.

[34] Pope SB. Turbulent Flows. third ed.. Cambridge University Press; 2000.

[35] Kazakov A, Frenklach M. DRM19 Mechanism.

[36] Yu R, Yu J, Bai X-S. An improved high-order scheme for DNS of low Mach number turbulent reacting flows based on stiff chemistry solver. J Comput Phys 2012;231(16):5504–21.

[37] Cohen SD, Hindmarsh AC, Dubois PF. CVODE, A Stiff/Nonstiff ODE Solver in C. Comput Phys 1996;10(2):138–43.

[38] Colin O, Ducros F, Veynante D, Poinsot T. A thickened flame model for large eddy simulations of turbulent premixed combustion. Phys Fluids 2000;12(7):1843–63.

[39] Charlette F, Meneveau C, Veynante D. A power-law flame wrinkling model for LES of premixed turbulent combustion part II: dynamic formulation. Combustion Flame 2002;131(1):181–97.

[40] Poinsot T, Veynante D. Theoretical and Numerical Combustion. third ed.. Cambridge University Press; 2001.

[41] Pappa A, Verhaeghe A, Bénard P, De Paepe W, Bricteux L. Adaptive mesh refinement towards optimized mesh generation for large eddy simulation of turbulent combustion in a typical micro gas turbine combustor. Energy 2024;131550.

[42] V. M, Bénard P, Lartigue G, R. M. Dynamic adaptation of tetrahedral-based meshes for the simulation of turbulent premixed flames. In: 17th international conference on numerical combustion. Aachen, Germany; 2019.

[43] Dapogny C, Dobrzynski C, Frey P. Three-dimensional adaptive domain remeshing, implicit domain meshing, and applications to free and moving boundary problems. J. Comput Phys. 2014;262:358–78.

[44] Bénard P, Balarac G, Moureau V, Dobrzynski C, Lartigue G, D'Angelo Y. Mesh adaptation for large-eddy simulations in complex geometries. Internat J Numer Methods Fluids 2016;81(12):719–40.

[45] Pappa A, Bricteux B, De Paepe W. Fast prediction of combustor stability limits in humidified micro gas turbines using hybrid 0D/1D model. In: ASME turbo expo 2023: GT2023-103904. 2023.

[46] Lewis B, von Elbe G. Stability and Structure of Burner Flames. J Chem Phys 1943;11(2):75–97.

[47] Eichler C, Sattelmayer T. Premixed flame flashback in wall boundary layers studied by long-distance micro-PIV. Exp Fluids 2012;52(2):347–60.

[48] Dugger GL. Flame stability of preheated propane-air mixtures. Ind Eng Chem 1955;47(1):109–14.

[49] Mohamadi M, Tahsini AM, Tavazohi R. Hydrogen addition impacts on flashback phenomenon in combustion chamber. Int J Hydrog Energy 2024;67:769–75.

[50] Von Elbe G, Mentser M. Further studies of the structure and stability of burner flames. J Chem Phys 1945;13(2):89–100.

[51] Aguilar JG, Æsøy E, Dawson JR. The influence of hydrogen on the stability of a perfectly premixed combustor. Combust Flame 2022;245:112323.

[52] Jowkar S, Shen X, Olyaei G, Reza Morad M. Hydrogen-enriched propane combustion in a lean premixed burner: LES study on flashback, emissions, and combustion instability. Fuel 2025;381:133377.

[53] Peters N. The turbulent burning velocity for large-scale and small-scale turbulence. J Fluid Mech 1999;384:107–32.

[54] Wang H, Luo K, Lu S, Fan J. Direct numerical simulation and analysis of a hydrogen/air swirling premixed flame in a micro combustor. Int J Hydrog Energy 2011;36(21):13838–49, 2010 Asian/APEC BioH2.

[55] Legrand N, Lartigue G, Moureau V. A multi-grid framework for the extraction of large-scale vortices in large-eddy simulation. J Comput Phys 2017;349:528–60.

[56] Welch P. The use of fast Fourier transform for the estimation of power spectra: A method based on time averaging over short, modified periodograms. IEEE Trans Audio Electroacoust 1967;15(2):70–3.

[57] Attili A, Luca S, Denker D, Bisetti F, Pitsch H. Turbulent flame speed and reaction layer thickening in premixed jet flames at constant karlovitz and increasing Reynolds numbers. Proc Combust Inst 2021;38(2):2939–47.

[58] Coulon V, Gaucherand J, Xing V, Laera D, Lapeyre C, Poinsot T. Direct numerical simulations of methane, ammonia-hydrogen and hydrogen turbulent premixed flames. Combust Flame 2023;256:112933.

[59] Rieth M, Gruber A, Williams FA, Chen JH. Enhanced burning rates in hydrogen-enriched turbulent premixed flames by diffusion of molecular and atomic hydrogen. Combust Flame 2022;239:111740, A dedication to Professor Kenneth Noel Corbett Bray.

[60] Choi J, Kim Hc, Lee Jg, Yoon Y. Flame structure and flashback process in hydrogen partially premixed flame. Exp Therm Fluid Sci 2025;168:111511.